THE JOURNAL OF PHYSICAL CHEMISTRY C

Article

Cite This: J. Phys. Chem. C 2019, 123, 16268−16280

pubs.acs.org/JPCC

Uniform Zn^{2+}-Doped BiOI Microspheres Assembled by Ultrathin Nanosheets with Tunable Oxygen Vacancies for Super-Stable Removal of NO

Fei Rao,[†] Gangqiang Zhu,[*,†] Mirabbos Hojamberdiev,[‡] Weibin Zhang,[§] Shiping Li,[†] Jianzhi Gao,[†] Fuchun Zhang,[∥] Yuhong Huang,[†] and Yu Huang[⊥]

[†]School of Physics and Information Technology, Shaanxi Normal University, Xi'an 710062, P.R. China

[‡]Fachgebiet Keramische Werkstoffe/Chair of Advanced Ceramic Materials, Institut für Werkstoffwissenschaften und -technologien, Technische Universität Berlin, Hardenbergstraße 40, 10623 Berlin, Germany

[§]School of Physics and Optoelectronic Engineering, Yangtze University, Jingzhou 434023, P.R. China

[∥]College of Physics and Electronic Information, Yan'an University, Yan'an 716000, P. R. China

[⊥]State Key Lab of Loess and Quaternary Geology (SKLLQG), Institute of Earth Environment, Chinese Academy of Sciences, Xi'an 710061, P.R. China

Supporting Information

ABSTRACT: Highly exposed active facets and surface oxygen vacancies (OVs) are beneficial for the photocatalytic removal of various harmful organic compounds. In this study, uniform Zn^{2+}-doped BiOI microspheres, assembled by ultrathin nanosheets with highly exposed {001} facets, with OVs were successfully synthesized for NO removal under visible light irradiation. The phase structure and chemical states are analyzed by means of X-ray diffraction and X-ray photoelectron spectroscopy, respectively. The transmission electron microscopy observations reveal that replacing Bi^{3+} with Zn^{2+} can lead to the increased exposure of the {001} facets. X-ray photoelectron and electron paramagnetic resonance spectroscopy results confirm that low-state Zn^{2+} increases the number of OVs, indicating that an increased number of OVs and a reduced thickness of the nanosheets can enhance the photocatalytic activity for the removal of NO. The photo-oxidative removal efficiency of NO over 3%Zn-BiOI reaches 53.6% and remains highly stable (52.9%) for up to 210 min under visible light irradiation. The calculation of interface adsorption confirms that OVs and Zn^{2+} can not only offer a donor energy level to extend the solar response range but also act as adsorption sites for low concentration of NO and O_2 to optimize the transmission capacity of surface charge carriers. Moreover, this work systematically explains the function of OVs and Zn^{2+} in the adsorption process of NO. The in situ Fourier transform infrared spectroscopy supports understanding of the photo-oxidative removal mechanisms of NO over Zn-BiOI: (i) the byproducts were bidentate nitrites (bi-NO_2^-), chelate nitrites (ch-NO_2^-), and bridging nitrites (br-NO_3^-) in the dark condition and (ii) the final products were bridging nitrites and bidentate nitrites (bi-NO_3^-) under visible light irradiation. OVs are found to play an important role both in the dark adsorption and photo-oxidative removal of NO by the 3%Zn-BiOI sample.

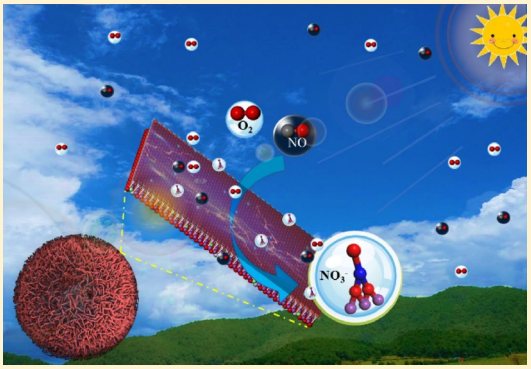

1. INTRODUCTION

With the development of modern industrial technology, the environment and human beings are more exposed to nitric oxide (NO), which has long been recognized as a hazardous pollutant.[1−3] NO can be easily oxidized to form toxic nitric dioxide (NO_2) that can pollute the environment, including water, soil, and atmosphere, and negatively impact human health.[3] Therefore, developing an effective, economic, and simple process of NO removal has attracted much attention in the field of environmental protection.[4−6] Recently, semiconductor-based photocatalysis has been regarded as an attractive alternative technology for NO removal because of its environmental friendliness and high efficiency.[4,7−9] Various bismuth-based semiconductors, such as Bi_2WO_6,[10] Bi_2O_3,[11] BiOBr,[12] $(BiO)_2SiO_3$,[13] $(BiO)_2CO_3$,[14] and Bi_2MoO_6,[15] have been studied due to their excellent photocatalytic performance.

The synthesis of semiconductor photocatalysts with highly exposed {001} facets has aroused scientific interest owing to special surface-dependent properties.[16] To date, a large number of works reported that the highly exposed {001}

Received: April 27, 2019
Revised: June 6, 2019
Published: June 9, 2019

DOI: 10.1021/acs.jpcc.9b03961
J. Phys. Chem. C 2019, 123, 16268−16280

facets can effectively improve the photocatalytic performance of photocatalysts, including BiOI,[2] $BiVO_4$,[17] $(BiO)_2CO_3$,[18] BiOBr,[19] and TiO_2.[20] As a novel semiconductor, bismuth oxyiodide (BiOI) has drawn much attention due to its smaller band gap (1.7−1.83 eV) and higher photochemical stability.[2,5] BiOI has positive $[Bi_2O_2]^{2+}$ layers and two slabs of negative I^-. The {001} facets of BiOI are parallel to the positive $[Bi_2O_2]^{2+}$ slabs. Due to the role of this special electric field, the photogenerated charge carriers move in the [001] direction.[21,22] Our previous work showed that the BiOI with highly exposed {001} facets has better photocatalytic performance than conventional BiOI.[2] In addition, the ultrathin nanosheets with highly exposed {001} facets promote a faster migration rate from the bulk to the surface by providing a shorter travel distance. Thus, if the BiOI nanosheets are synthesized with highly exposed {001} facets, they should exhibit higher photocatalytic performance under visible light irradiation. Previously, several studies have shown that metal ion doping can control the growth direction of the crystal to regulate the thickness of the nanosheet because metal ions on the surface of the crystal can limit or promote the facet growth.[7,12,22−24] Therefore, metal ion doping is a promising approach to control the thickness of nanosheets.

Regarding the doping method, the crystal defects of the photocatalyst are generated by controlling the chemical state of the doped metal ion that greatly affects the photocatalytic activity.[25] Doping of unbalanced valence ions can induce the formation of some oxygen vacancy (OV) defects. For example, Huang et al.[26] found that Fe^{3+} doping in the $SrTiO_3$ lattice replaced Ti^{4+}, inducing the formation of oxygen vacancies and promoting the photocatalytic activity.[26] Tripathi and coworkers[27] pointed out that the Sr^{2+} doping in SnO_2 nanoparticles may facilitate the separation of charge carriers through the creation of OVs. As a typical defect, oxygen vacancy has been a highlight in various photocatalytic processes, such as water treatment, CO_2 reduction,[3,28] and N_2 fixation.[29] OVs are also known to provide trapping sites for photogenerated electrons and to inhibit the recombination of photogenerated charge carriers.[11] Furthermore, several reports described that OVs can adjust the band structure to increase solar light absorption. More importantly, OVs can serve as active sites to adsorb more oxygen molecules to form superoxide radicals ($\bullet O_2^-$), boosting the photocatalytic performance.[3] It has been proven that the ionic radius of Zn^{2+} (0.074 nm) is smaller than the ionic radius of Bi^{3+} (0.103 nm).[17,20−22] Some studies concluded that Zn^{2+} can effectively control the growth of crystals. The morphology of the photocatalyst progressively changes from truncated rods to sharp needles by the effect of Zn^{2+} doping. For example, Liu et al.[30] reported that the morphology of the SnO_2 nanostructures can be changed from blunt nanorods to acute nanoneedles by the effect of Zn^{2+} doping. This indicates that Zn^{2+} doping can indeed affect the growth direction and surface energy of the crystal. Therefore, Zn^{2+} can be a good dopant that can not only induce the formation of OVs but also reduce the thickness of nanosheets to improve the ratio of {001} facets. In other words, the incorporation of Zn^{2+} can expose more active facets with a large number of OVs.

The internal electronic structure, the number of OVs, the thickness of the structure, and highly exposed crystal facets are crucial factors influencing the photocatalytic activity of the photocatalyst. Thus, it is necessary to construct a superior photocatalyst by assembling ultrathin nanosheets with highly exposed {001} facets, higher content of OVs, and excellent transport capability of surface electrons. In this study, we aim at synthesizing the uniform Zn^{2+}-doped BiOI microspheres by assembling ultrathin nanosheets with highly exposed {001} facets and a large number of OVs under solvothermal conditions. The synthesized materials are investigated for the photo-oxidative removal of NO under visible light irradiation. Particularly, we use in situ Fourier transform infrared spectroscopy (FTIR) to understand the dark adsorption and photo-oxidative removal mechanisms of NO over the synthesized materials.

2. EXPERIMENTAL SECTION

2.1. Synthesis. All chemical reagents received from Aladdin Reagents Co., Ltd. (China) were of analytical grade and used without further purification. Uniform 2−5% Zn^{2+}-doped BiOI microspheres by assembling ultrathin nanosheets with highly exposed {001} facets and a large number of OVs were synthesized by a one-step solvothermal method. First, 1.3824 g of $Bi(NO_3)_3{\cdot}5H_2O$ was added into 20 mL of ethylene glycol, and then 0.0172, 0.0257, 0.0343, or 0.0429 g of $Zn(NO_3)_2{\cdot}6H_2O$ was introduced. Afterward, 0.501 g of KI was added into the above mixture and stirred until a clear solution was formed. Finally, the reaction solution was transferred into a Teflon-lined stainless steel autoclave and maintained at 160 °C for 12 h. The resulting precipitate was collected and washed with deionized water and ethanol repeatedly and then dried at 70 °C in air. Pure BiOI microspheres were synthesized in parallel by applying identical synthesis conditions without adding $Zn(NO_3)_2{\cdot}6H_2O$. The OVs-BiOI photocatalyst was synthesized by a UV irradiation method, and the detailed process is given in the Supporting Information.

2.2. Characterization. The crystalline phases were identified using X-ray powder diffraction (XRD, Bruker D8 Advance) with Cu Kα1 (1.5418 Å) radiation at a scanning rate of $10°{\cdot}min^{-1}$ in the 2θ range of 10−80°. The morphology and nanostructure of samples were observed by field emission scanning electron microscopy (FESEM, Nova NanoSEM 450, FEI) and spherical aberration-corrected transmission electron microscopy (ac-TEM, Titan Cubed Themis G2 300), respectively. The UV−vis absorption spectra were acquired using a UV−vis−NIR spectroscopy (Cary 5000, Agilent) using $BaSO_4$ as the background over a range of 200−1200 nm. The photoluminescence (PL) spectra were obtained by a Fluoromax-4 spectrophotometer (HORIBA Scientific, excited at λ = 480 nm). The specific surface areas and pore size distributions were estimated by Brunauer−Emmett−Teller (BET) and Barrett−Joyner−Halenda (BJH) methods using the N_2 adsorption−desorption isotherms measured with a BELSORP-max-II. The X-ray photoelectron spectroscopy (XPS) data were obtained using an ESCALAB MKII spectrometer (VG Scienta) with Al Kα radiation (1486.6 eV).

The X-band electron spin-resonance (ESR) spectra were recorded on an ER200-SRC (Bruker) at room temperature. For the ESR measurements, the sample was prepared by mixing 0.05 g of the photocatalyst in a 50 mM 5,5′-dimethyl-1-pirroline *N*-oxide (DMPO) solution in aqueous dispersion for DMPO−$^{\cdot}OH$ and in methanol dispersion for DMPO−$^{\cdot}O_2^-$ under visible light irradiation (300 W Xe lamp) with a 420 nm filter. The details of the photocatalytic activity test for NO removal, in situ FTIR study of photo-oxidation of NO, density functional theory (DFT) calculations, and related analysis

DOI: 10.1021/acs.jpcc.9b03961
J. Phys. Chem. C 2019, 123, 16268−16280

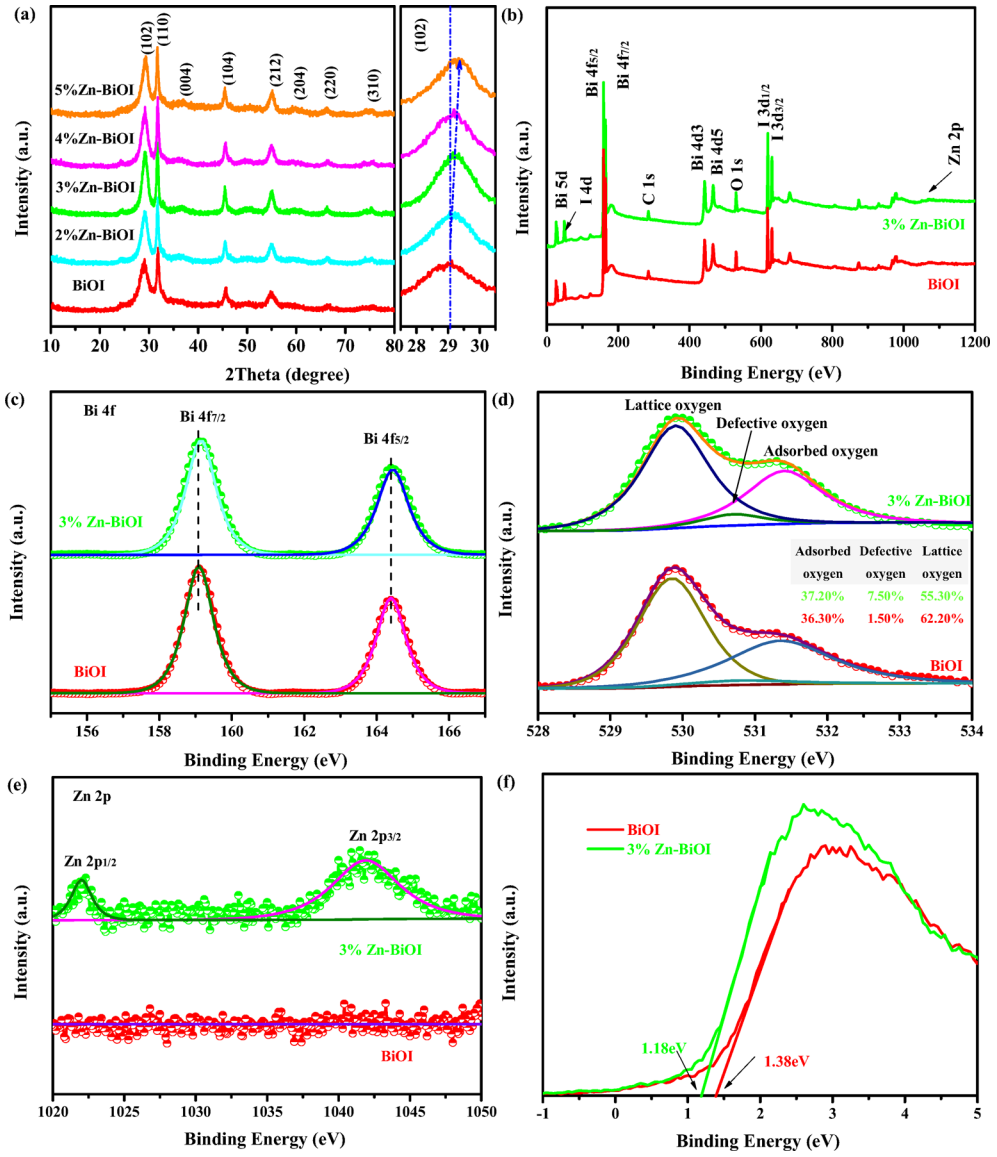

Figure 1. (a) XRD patterns of the as-synthesized BiOI and 2−5% Zn-BiOI samples, (b) XPS survey spectra of BiOI and 3%Zn-BiOI samples, high-resolution XPS spectra of (c) Bi 4f, (d) O 1s, and (e) Zn 2p of BiOI and 3%Zn-BiOI samples, and (f) VB XPS spectra of BiOI and 3%Zn-BiOI.

about the BiOI sample with only OVs are given in the Supporting Information.

3. RESULTS AND DISCUSSION

3.1. XRD and XPS. The phase structure and chemical states of elements of the synthesized samples were analyzed by XRD and XPS, respectively. The crystal structures of BiOI and Zn-BiOI are shown in Figure S1, revealing that BiOI has positive $[Bi_2O_2]^{2+}$ layers and two slabs of negative I^-. Figure 1a shows the XRD patterns of the BiOI and Zn-BiOI samples. The XRD patterns of 2−5% Zn^{2+}-doped BiOI samples can be readily indexed to tetragonal BiOI (ICDD PDF# 10−0445). Clearly, the sharp diffraction peaks at 2θ = 29.6, 31.6, 45.3, and 55.1° correspond to the (102), (110), (200), and (212) crystallographic planes of tetragonal phase BiOI, respectively. Moreover, the intensity of the (110) diffraction peak is higher than that of the (102) diffraction peak, suggesting that the as-synthesized BiOI and Zn^{2+}-BiOI crystals have a special anisotropy growing along the {001} crystallographic facets.[31] As shown in Figure 1a, the (102) diffraction peak was slightly shifted toward higher 2θ angles with increasing doping concentration of Zn^{2+}, confirming the doping of Zn^{2+} in the BiOI lattice. Interestingly, no impurity phases are observed, indicating the stability of BiOI upon Zn^{2+} doping.

To further comprehend the elemental compositions, chemical states, and the presence of zinc, XPS analysis was performed using BiOI and 3%Zn-BiOI samples. Figure 1b shows the XPS survey spectra, indicating the presence of Bi, O, and I elements in both samples and the Zn element in 3%Zn-BiOI. The high-resolution XPS spectra of Bi 4f, O 1s, and Zn 2p are shown in Figure 1c−e. As shown in Figure 1c, the Bi $4f_{7/2}$ and Bi $4f_{5/2}$ peaks are centered at 158.9 and 164.2 eV, respectively, confirming the existence of Bi^{3+}.[16] A minor shift of the Bi 4f peak emerged owing to the change in the electronic distribution around the Bi atoms. That is, the neighboring Zn^{2+} and OVs for Bi^{3+} atoms have higher electron-attracting ability. The differential charge distribution around Bi atoms was estimated using the DFT calculations to determine the reason for this charge transfer trend. The high-resolution XPS spectra of O 1s of BiOI and 3%Zn-BiOI are shown in Figure 1d.

DOI: 10.1021/acs.jpcc.9b03961
J. Phys. Chem. C 2019, 123, 16268−16280

According to a previous report,[32] the main peak at 529.9 eV can be assigned to the coordination of oxygen in Bi−O, whereas the secondary peak at 530.7 eV may be attributed to the coordination of OVs.[33] In Figure 1d, the area ratio of the fitting peaks shows that the relative contents of OVs in the surface are ∼1.5 and 7.5% for BiOI and 3%Zn-BiOI samples, respectively. The peak at 531.4 eV is related to the adsorbed oxygen on the surface of samples.[33,34] The peaks at 619.0 and 631.0 eV are attributed to I $4f_{7/2}$ and I $4f_{5/2}$ (Figure S2),[35] respectively. As for the high-resolution Zn 2p spectrum of 3% Zn-BiOI in Figure 1e, two peaks are observed at 1044.4 and 1022.0 eV, which can be assigned to Zn $2p_{3/2}$ and Zn $2p_{1/2}$,[30] respectively. It further proves that Zn was successfully incorporated into the BiOI lattice. Additionally, Figure 1f shows the valence band (VB) XPS spectra of the synthesized samples. It is evident that the VB edges of BiOI and 3%Zn-BiOI are located at 1.38 and 1.18 eV, respectively, suggesting that Zn^{2+} doping can adjust the electronic structure, resulting in a decrease of the band gap.

3.2. SEM and TEM. Figure 2a,b shows that the 3%Zn-BiOI sample has a microspherical morphology with a diameter of

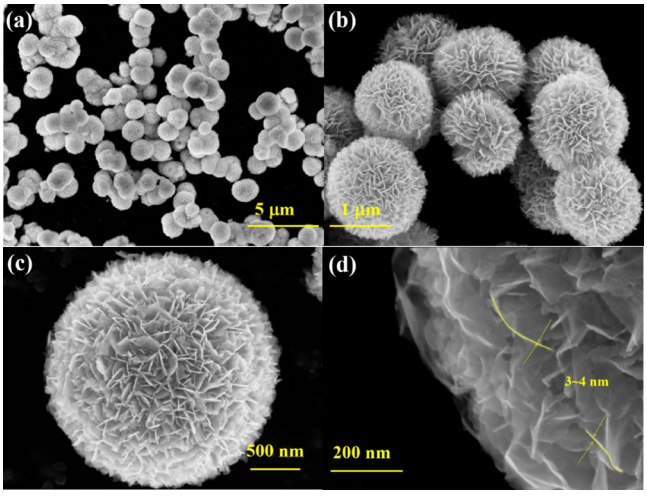

Figure 2. SEM images of 3%Zn-BiOI microspheres.

1∼3 μm. The SEM image of pure BiOI in Figure S3a indicates that the doping of Zn^{2+} does not affect the morphology of the microspheres in micron size. However, Figure 2c confirms that the microspheres at the nanoscale consist of numerous ultrathin nanosheets with a thickness of 3−4 nm. In Figure S3b, the thickness of pure BiOI nanosheets is twice (7−11 nm) that of Zn^{2+}-doped BiOI, suggesting that the reduction in the nanosheet thickness resulted from Zn^{2+} doping.

In order to further investigate the nano- and microstructures of the synthesized samples, TEM observations were performed. As shown in Figure 3 and Figure S4, 3D flower-like 3%Zn-BiOI microspheres with a diameter of 1.4−3.0 μm are assembled by ultrathin nanosheets with a thickness of 3−4 nm. The crystal lattice of the 3%Zn-BiOI nanosheets is represented by HRTEM images in Figure 3b. Clearly, two mutually perpendicular crystal faces with the lattice spacings of 0.279 and 0.284 nm correspond to the (110) and (1−10) crystallographic planes of tetragonal BiOI, respectively. Both of these crystallographic planes belong to the {001} family. Furthermore, the (110) and (001) lateral high-angle annular dark-field scanning transmission electron microscopy

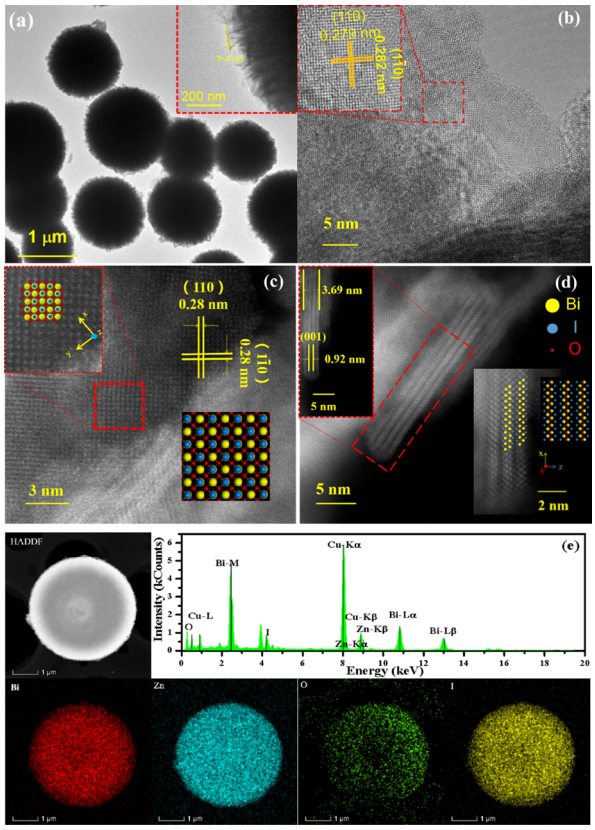

Figure 3. (a) TEM image, (b) HRTEM image, (c, d) HAADF images with corresponding atomic structures, and (e) EDS elemental mapping images of 3%Zn-BiOI (scale bar is 1 μm).

(HAADF-STEM) images are shown in Figure 3c,d. Clearly, the HAADF-STEM images reveal the crystal structure of Zn-BiOI. The intensity of the HAADF image is proportional to the signal intensity of the atoms, and the signal intensity is related to the atomic number. That is, the larger the atomic number, the stronger the signal is and the brighter the dots are in the HAADF images.[36] It is worth noting that oxygen atoms are invisible in the HAADF-STEM images.[37] Hence, the high brightness spots are indexed to Bi atoms, whereas the spots with lower brightness represent I atoms. Since the Bi and Zn atoms cannot be completely distinguished, the Zn atoms, which should theoretically exist at the Bi position, are represented by Bi. As shown in Figure 3c, the arrangement of atoms in the cross section of (001) is consistent with the schematic diagram of the BiOI crystal structure. In Figure 3c, the atoms are arranged in a matrix. The distance between the Bi atoms and their way of arranging confirm that the highly exposed facet is (110). Therefore, the highly exposed {001} facets are directly proven. As shown in Figure 3d, the Zn-BiOI microspheres consist of nanosheets with a thickness of 3.7 nm, and the interstitial spacing is approximately 0.92 nm, corresponding to the (001) crystallographic plane. It is clearly shown that the ultrathin nanosheet includes four alternating $[Bi_2O_2]^{2+}$ and I^- layers. In addition, the distribution of these atoms along the c axis is identical to the atomic spatial arrangement of the BiOI (001) plane illustrated in Figure 3d. As shown in Figure S5, the specific surface area increased from 61.174 to 76.134 $m^2 \cdot g^{-1}$ when BiOI was doped with 3% Zn. It can be concluded that the doping of Zn^{2+} can effectively inhibit the growth rate of the BiOI crystal in the c axis direction,

DOI: 10.1021/acs.jpcc.9b03961
J. Phys. Chem. C 2019, 123, 16268−16280

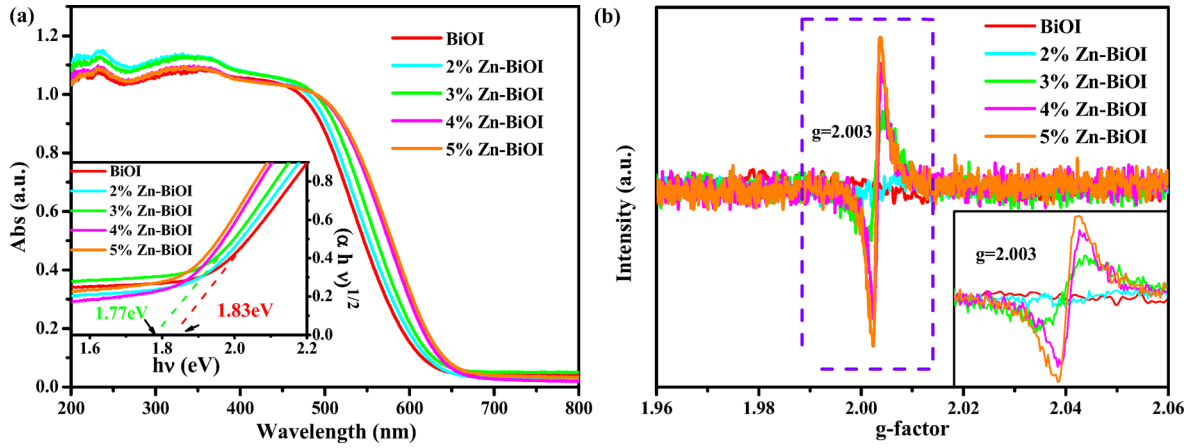

Figure 4. (a) UV−vis absorption spectra (inset image of $h\nu$ vs $(\alpha h\nu)^{1/2}$) and (b) EPR spectra of BiOI and Zn-BiOI samples.

reducing the thickness of nanosheets and exposing more {001} crystallographic planes. Additionally, the elemental composition of the 3%Zn-BiOI sample was analyzed by energy-dispersive X-ray spectroscopy (EDS). As shown in Figure 3e, Zn and Cu were also detected in addition to Bi, O, and I elements. The Cu signal in the EDS spectrum is from the sample holder, and the Zn signal comes from the doped Zn^{2+} in the BiOI sample. The EDS element mapping images clearly show that the Zn, Bi, O, and I elements are uniformly distributed over the observed area.

3.3. UV−Vis, EPR, and Band Structure. Figure 4a shows the UV−vis absorption spectra of the pure BiOI and Zn-BiOI samples. The absorption edge is observed in the region of 600−650 nm, indicating that electrons are excited from the valence band to the conduction band by light irradiation.[38] It is also observed that the absorption edge slightly red-shifted with increasing Zn content in BiOI. The band-gap values are ∼1.83 and 1.77 eV for BiOI and 3%Zn-BiOI, respectively. Combined with the valence band position in the XPS spectra (Figure 1f), the conduction band edges of BiOI and 3%Zn-BiOI were estimated to be at −0.65 and − 0.59 eV, respectively. The narrower band gap of Zn-BiOI is attributed to the increased number of OVs and level of Zn^{2+} doping. The contribution of OVs and Zn^{2+} to the electronic structure is further investigated by DFT calculations, explaining the essential reason for optimizing light absorption.

In the high-resolution XPS spectra of O 1s (Figure 1d), the signal of OVs in the BiOI and 3%Zn-BiOI samples is detected. Further, electron paramagnetic resonance (EPR) spectroscopy was applied to confirm the existence of OVs in the BiOI and 3%Zn-BiOI samples.[32] EPR can not only probe the defects directly with high sensitivity but also determine the type of defects by a g factor value. As shown in Figure 4b, BiOI samples show a gradient appearance of a symmetrical EPR signal at g = 2.003, whereas 5%Zn-BiOI shows the strongest signal at the same location. The remarkable symmetric peaks observed at $g \approx 2.003$ are typical oxygen vacancy-associated peaks, and the intensity of this peak has a positive correlation with the amount of OVs.[39] Obviously, the concentration of OVs in the synthesized samples gradually increased with increasing Zn content. The Zn^{2+}-doped BiOI samples show a stronger signal for OVs because some of the Bi^{3+} was replaced by Zn^{2+}, and within the doping of 5% atomic ratio, the concentration of OVs also increases as the number of replaced Bi^{3+} ions increases. It is well known that the dopant with lower valency can create an effective positive charge at the anion lattice,[40] forming the OVs. Based on the above results, it can be concluded that the doping of Zn^{2+} can not only expose more active facets but also change the concentration of OVs.

The band structures and partial/total densities of states (P/TDOS) were calculated by the DFT method to determinate the effects of OVs and Zn^{2+} on highly exposed {001} facets. As shown in Figure 5a, pure BiOI is an indirect semiconductor, and its conduction band minimum (CBM) and valence band maximum (VBM) are located at different high-symmetry points, indicating that BiOI possesses a good electron−hole separation ability.[41,42] The calculated band gaps of pure and Zn^{2+}-doped OV-rich BiOI samples are 1.78 and 1.67 eV, respectively. These theoretically estimated band gaps are slightly smaller than the experimentally measured band gaps because of the limitation of generalized gradient approximation (GGA).[43] A decrease in the band gap is attributed to the effects of Zn^{2+} doping and OVs. It is worth noting that the CBM and VBM of Zn^{2+}-doped BiOI are more negative (Figure 5c), which is consistent with the VB-XPS data. The negative CBM indicates that the Zn^{2+}-doped BiOI has a stronger oxidizing ability than pure BiOI.

In Figure 5b, the electronic states of the VB of pure BiOI in the energy range between −5.65 and 0.02 eV are mainly ascribed to the strong I 5p states and a small number of O 2p and Bi 6p electrons. The deep VB in the energy range between −7.61 and − 10.00 eV mainly comes from Bi 6s and I 5s states. However, the VBM and CBM shifted to positive energy. Importantly, Figure 5c shows that an intermediate band emerges in the intermediate of the band gap after the introduction of Zn^{2+} and OVs. The PDOS reveals that the doping states mainly originate from O 2p (Figure 5d). In fact, the intermediate band introduced by OVs plays an important role in the photocatalytic process. An original band gap was divided into two parts by the extra band. Simultaneously, the intermediate band acts as a "step" to absorb lower-energy photons.[44,45] Some of the excited electrons in the CB during the photocatalytic process are trapped by the half-filled O 2p state, which increases the separation ability of photogenerated charges and promotes the photon absorption ability of the photocatalyst. Thus, the reduction in the band gap was caused by the doping level of OVs. In addition, the deep VB contribution of Zn in the BiOI structure indicates that Zn^{2+} can introduce OVs without adjusting the positions of CB and VB edges in BiOI.

DOI: 10.1021/acs.jpcc.9b03961
J. Phys. Chem. C 2019, 123, 16268−16280

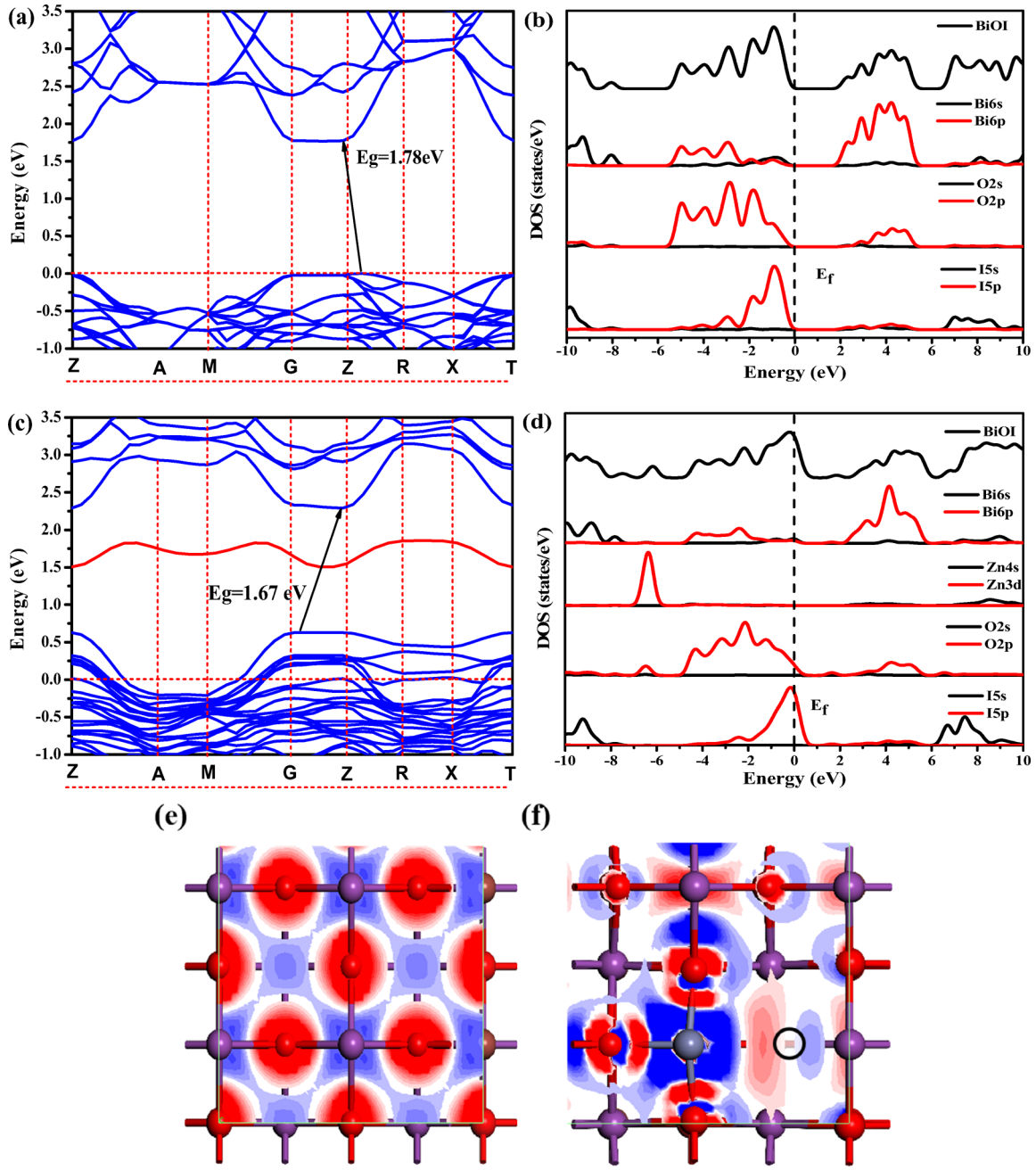

Figure 5. (a, b) Band structures, (c, d) partial/total densities of states (P/TDOS) and (e, f) charge difference distributions of BiOI and 3%Zn-BiOI.

Figure 5e,f reveals charge difference distributions of BiOI and 3%Zn-BiOI with OVs to understand the charge transfer trend in the photocatalysts. The black, blue, and red circles represent OVs, charge exhaust, and charge accumulation, respectively. As shown, the tendency of charge in pure BiOI is from Bi to O atoms, of which the flow mode is in a "dynamic balance" status; however, this balance was changed with the intervention of Zn^{2+} and OVs. The OV sites indicate strong accumulation areas of electrons and intensively dissipate areas around the Zn atom in the Zn^{2+}-doped BiOI compared to those in pure BiOI. This indicates that electrons are easily trapped by OVs, limiting the recombination of photogenerated electrons and holes. Moreover, a change of the charge distribution around the Bi atoms was observed because electrons have a tendency to move from the Bi site to OVs. This tendency effectively provides evidence for the minor shift of Bi 4f peaks in the high-resolution XPS spectra of Bi. In short, this special transfer of electrons around the OVs should promote the removal efficiency of NO on the surface of the 3% Zn-BiOI sample under the dark condition.

3.4. Photo-Oxidative Removal of NO. The photocatalytic activities of the as-synthesized samples were evaluated by the photo-oxidative removal of NO under visible light irradiation ($\lambda \geq 420$ nm). Figure 6a shows the change in NO concentration (C/C_0) versus irradiation time in the presence of different samples. Obviously, pure BiOI exhibits a lower photocatalytic activity (37.12% removal efficiency) due to the high recombination rate of photogenerated charge carriers. The photocatalytic activity for NO removal was improved by Zn^{2+} doping, and the removal efficiencies of NO by 2%Zn-

DOI: 10.1021/acs.jpcc.9b03961
J. Phys. Chem. C 2019, 123, 16268−16280

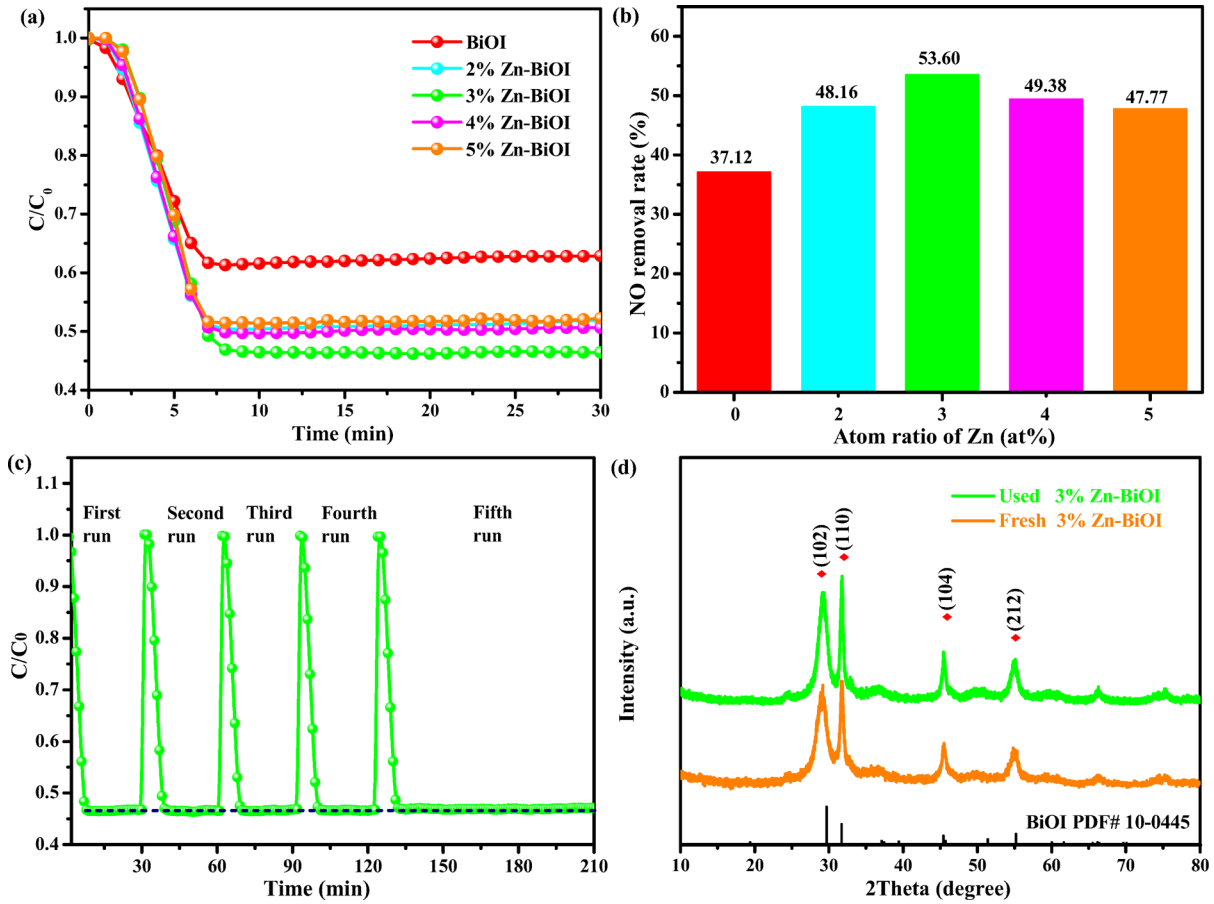

Figure 6. (a, b) Photo-oxidative removal of NO by pure BiOI and Zn^{2+}-doped BiOI samples, (c) cycle photocatalytic performance of 3%Zn-BiOI, and (d) XRD patterns of 3%Zn-BiOI before and after the photocatalytic reaction.

BiOI, 3%Zn-BiOI, 4%Zn-BiOI, and 5%Zn-BiOI samples were found to be 48.16, 53.60, 49.38, and 47.77% (Figure 6b), respectively. Particularly, the 3%Zn-BiOI sample shows the highest photocatalytic activity for NO removal. This high photocatalytic activity for NO removal presumably resulted from the OVs, highly exposed {001} facets, and efficient charge transfer. Additional experiments were run to evaluate the stability and recyclability of the 3%Zn-BiOI photocatalyst. The photo-oxidative removal efficiency of NO was ~53.6, 53.5, 53.4, 53.3, and 52.9% in five consecutive cycles (Figure 6c). Even though the irradiation time was extended to 90 min, the removal efficiency of NO over the 3%Zn-BiOI sample could still maintain a superior stability (52.9%) in the fifth cycle. To further confirm the stability of 3%Zn-BiOI for photo-oxidative removal of NO, the sample after a photocatalytic reaction was examined by XRD. The XRD patterns of the 3%Zn-BiOI samples before and after the photocatalytic reaction are shown in Figure 6d, implying that the crystal structure of 3%Zn-BiOI was stable during the photocatalytic process. For comparison, the BiOI sample only with OVs and without Zn^{2+}-doping was also synthesized, and the results of characterization are given in the Supporting Information. In Figure S7b, the photo-oxidative removal efficiency for NO of OVs-BiOI was reduced by 15% after five consecutive cycles. Such reduction is attributed to the instability of photoinduced OVs during the photocatalytic process. This phenomenon is consistent with previous reports,[26] describing the possibility of using the UV irradiation method to create OVs. Thus, the as-synthesized Zn^{2+}-BiOI photocatalyst can be used in practical applications in the future as a stable and recyclable photocatalyst.

3.5. Photoinduced Charge Separation. It is well known that the photocatalytic activity directly depends on the competition between the charge separation and recombination processes. In order to investigate the effect of OVs on photocatalytic activity of the BiOI photocatalysts, photoluminescence (PL) spectroscopy was used. In Figure 7a, pure BiOI has a stronger emission peak at ~652 nm with an excitation wavelength of 480 nm than 3%Zn-BiOI sample, indicating the higher recombination rate of photogenerated charge carriers in the former in comparison to the latter one. The emission intensity of the 3%Zn-BiOI sample was reduced, indicating that the recombination of photogenerated charge carriers was greatly restrained due to the intermediate band introduced by OVs. The photocurrents of pure BiOI and 3% Zn-BiOI electrodes were measured periodically by switching on/off the light source. As shown in Figure 7b, the photocurrent signals of both samples were detected when the light was turned on, and a rapid decay was observed when the light was off. It can be seen that the photocurrent increased after Zn^{2+} doping into BiOI. The transfer of photogenerated electrons was further studied by electrochemical impedance spectroscopy (EIS), and the results are plotted in Figure 7c. The smallest radius of curvature of the 3%Zn-doped BiOI electrode, both in the dark and under irradiation, indicates that the introduction of Zn^{2+} significantly reduced the charge transfer resistance. The above results also indicated that the optimized concentration of Zn^{2+} is favorable for charge

DOI: 10.1021/acs.jpcc.9b03961
J. Phys. Chem. C 2019, 123, 16268−16280

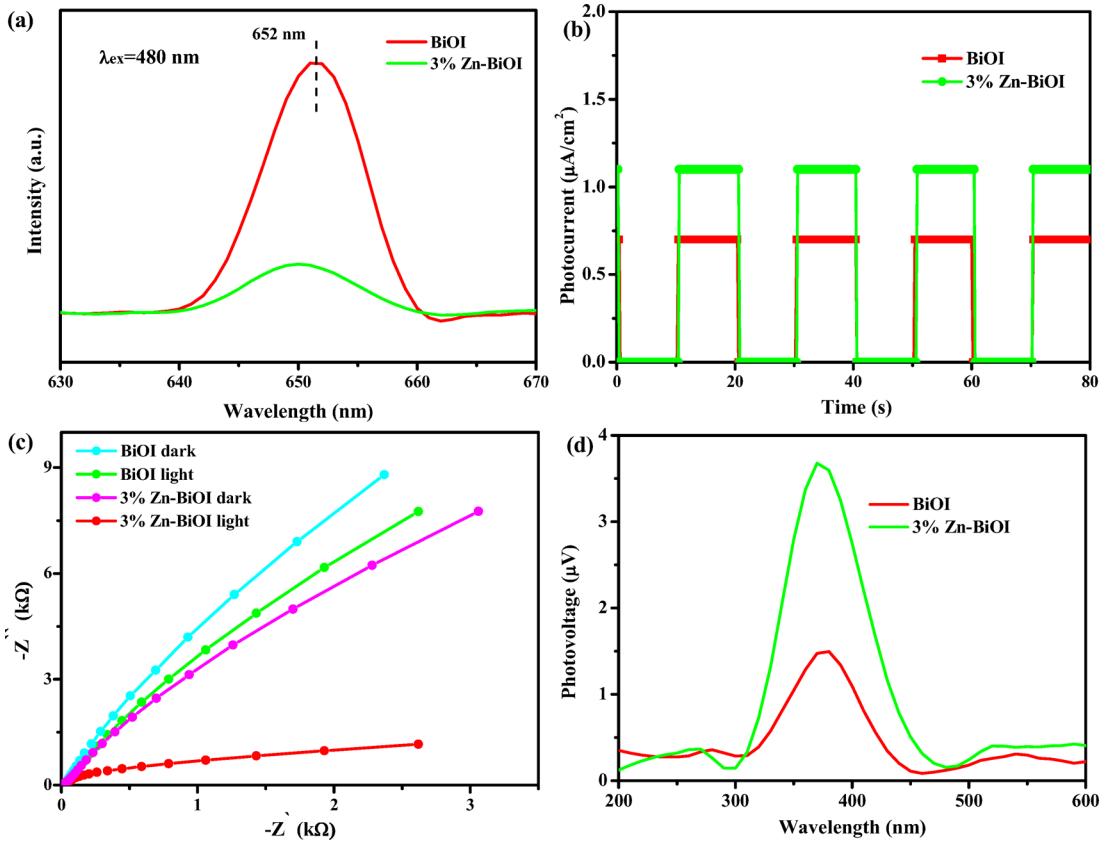

Figure 7. (a) PL spectra, (b) photocurrents, (c) Nyquist plots, and (d) SPS spectra of pure BiOI and 3%Zn-BiOI samples.

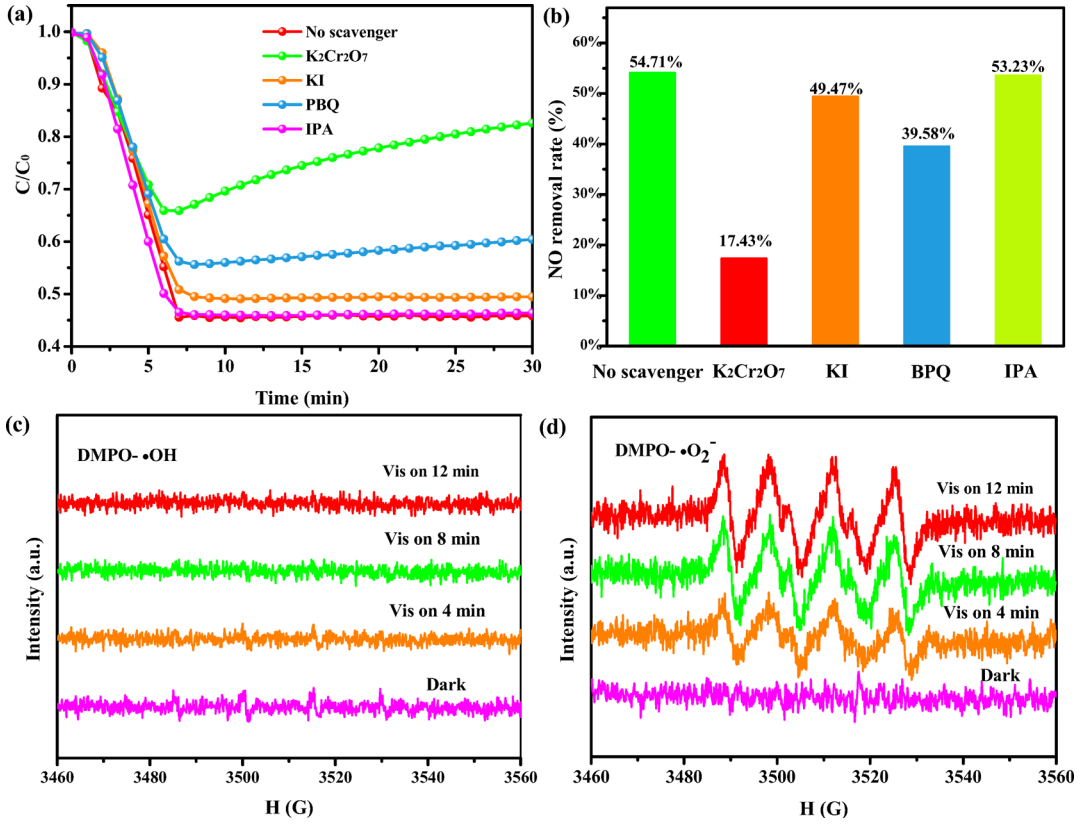

Figure 8. (a, b) Photocatalytic activities in the presence of various scavengers and (c, d) DMPO-ESR spectra of the 3%Zn-BiOI sample under visible light irradiation.

DOI: 10.1021/acs.jpcc.9b03961
J. Phys. Chem. C 2019, 123, 16268−16280

separation in the BiOI nanostructures. Surface photovoltage spectroscopy (SPS) is an advantageous technique to study the surface physical properties of solid materials and the charge transfer process between different interfaces. Also, SPS can quickly and nondestructively measure the surface properties of semiconductors.[46] The separation and transfer processes of photogenerated charge carriers on the surface of the synthesized samples can also be studied using SPS. Under identical measurement conditions, a stronger SPS signal indicates higher separation efficiency of photogenerated charge carriers. Figure 7d shows the SPS spectra of the as-synthesized samples. As shown, 3%Zn-BiOI has a clear SPS signal upon irradiation with wavelengths ranging from 300 to 490 nm. Interestingly, this wavelength range is much broader than that of pure BiOI (310 to 400 nm). The SPS response is also related to the surface defects. The wider SPS signal of 3%Zn-BiOI is attributed to the presence of surface defects in the form of OVs.[47] The greater the relative amount of OVs, the stronger the SPS signal intensity is. The OVs can effectively capture photogenerated electrons, and the captured electrons combine with O_2 to activate oxygen via the bridge function of OVs. In this process, OVs play an important role in the transfer of carriers, which is consistent with photodegradation results.

3.6. Trapping Experiments and ESR. In order to probe the mechanism of NO removal over 3%Zn-BiOI with OVs, the trapping experiments were performed. It is obvious that the addition of $K_2Cr_2O_7$ and PBQ significantly reduced the photocatalytic activity for NO removal, while the inhibition effect was imposed by KI. IPA was less effective than $K_2Cr_2O_7$ and PBQ. Figure 8b shows that the photocatalytic efficiencies for NO removal are 54.71, 17.43, 49.47, 39.38, and 53.23% in the presence of no scavenger, $K_2Cr_2O_7$, KI, PBQ, and IPA, respectively, implying that photogenerated electrons and $^{\cdot}O_2^-$ played the most important role in photo-oxidative removal of NO. The photogenerated holes had less impact on photocatalytic activity, whereas $^{\cdot}OH$ was nearly ineffective in the photocatalytic reaction. In general, electron spin resonance (ESR) spectroscopy is used to detect reactive oxygen species. In ESR spectroscopy, DMPO spin-trapping adducts are utilized to capture superoxide radicals (DMPO−$^{\cdot}O_2^-$) in methanol and hydroxyl radicals (DMPO−$^{\cdot}OH$) in aqueous solution. As shown in Figure 8c,d, no featured signals were detected in the dark. Nevertheless, only several strong characteristic peaks of DMPO−$^{\cdot}O_2^-$ can be clearly seen upon visible light irradiation. The number of active species was increased with extending irradiation time, indicating that the Zn^{2+}-doped BiOI cannot generate $^{\cdot}OH$ but can produce $^{\cdot}O_2^-$ species. Combining the results of scavenger experiments, photogenerated e^- and $^{\cdot}O_2^-$ species play an important role, while photogenerated holes play a secondary role in the photo-oxidative removal process of NO. Moreover, $^{\cdot}OH$ species do not contribute to the NO removal process due to the absence of $^{\cdot}OH$ radical species. According to the VB-XPS results, the standard redox potential of $H_2O/^{\cdot}OH$ is 2.27 eV, and only when the VBM is lower than this potential, OH^- can be oxidized to $^{\cdot}OH$. This clearly explains why there was no $^{\cdot}OH$ species generated in the trapping experiments and ESR measurements.

3.7. Reactant Activation. The adsorption of NO + O_2 on the photocatalyst surface is a crucial and first step for a gas−solid photocatalytic reaction. The metal ions and OVs on the photocatalyst surface are regarded as the traps for electrons and gases. To further investigate the interaction between the surface of 3%Zn-BiOI, which contains Zn, OVs and highly exposed {001} facets, and gaseous NO and O_2, the adsorption of NO + O_2 molecules on the surface of 3%Zn-BiOI was calculated by DFT method. The geometry optimization of the crystal models of Zn^{2+}-doped BiOI is shown in Figure S8. It shows that the presence of Zn + OVs can result in the change of the BiOI lattice plane at the interface of BiOI and gases, which is anticipated to affect the transfer of photogenerated charge carriers at the interfaces. Generating the active radicals is important for the photo-oxidative removal of NO. The OVs located on the photocatalyst surface are considered effective activation sites for O_2. Figure 9a,b show the charge density

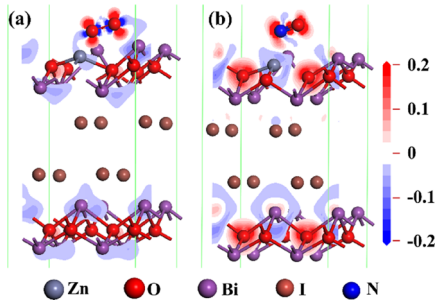

Figure 9. Adsorption of (a) O_2 and (b) NO on 3%Zn-BiOI.

difference images of the NO and O_2 molecules interacting with Zn^{2+} doped in BiOI. The blue and red areas indicate the charge exhaust and charge accumulation. The changes of the bond lengths of NO and O_2 during the entire process are given in Table S2. It is shown in Figure 9a that there is a strong interaction between O_2 and the photocatalyst surface. Clearly, electrons have a tendency of moving from BiOI to O_2. The length of the O−O bond (1.476 Å) was extended, implying that the OVs on the highly exposed {001} facets are the most beneficial configuration for O_2 adsorption. Moreover, the OVs can activate O_2 via transferring electrons from BiOI to O_2, promoting the formation of O_2^-.[48,49] In Figure 9b, the calculation results of the adsorption of NO over the {001} facets of Zn^{2+}-doped BiOI are shown. The Zn^{2+}-doped BiOI was the most favorable configuration for the adsorption of NO as indicated by a largely extended N−O bond (1.221 Å) because the adsorption of NO molecules is accompanied by an electron transfer from Zn sites to NO species, while electrons are donated by OVs. In other words, Zn sites play a bridge role, transferring electrons from BiOI to NO species, and OVs play a donor role, offering active electrons during the adsorption process. When the co-adsorption of NO and O_2 molecules on the surface of Zn^{2+}-BiOI takes place, the formed O_2^- can immediately participate in the oxidation process of NO without irradiation.[50] This observation will be further proven by in situ FTIR studies under the dark condition. In addition, under visible light irradiation, the built-in electric field influences photogenerated electrons, transferring to the {001} facets. The transfer of photogenerated electrons toward O_2 is accelerated by Zn^{2+} and OVs on the {001} facets, and an increased quantity of $^{\cdot}O_2^-$ is formed subsequently, improving the photocatalytic activity of Zn^{2+}-doped BiOI. To explain the superior stability during the photocatalytic reaction, the NO adsorption on the BiOI and Zn^{2+}-doped BiOI without OVs is shown in Figure S9. Combined with Zn^{2+}-doped BiOI with OVs, the adsorption of NO molecules indicates that the photo-oxidation process of NO mainly takes place on Zn^{2+} or Bi^{3+}

DOI: 10.1021/acs.jpcc.9b03961
J. Phys. Chem. C 2019, 123, 16268−16280

sites not OV sites. Thus, the oxidation stability of OVs would not be disturbed with the photocatalytic process proceeds. As shown above, the Zn^{2+}-doped BiOI sample shows superior stability under continuous photo-oxidative removal of NO for 210 min.

3.8. In Situ FTIR Study. To investigate the mechanisms of the photo-oxidative removal of NO by Zn-doped BiOI, in situ Fourier-transform infrared spectroscopy (in situ FTIR) was used to simulate the monitoring of the time-dependent photocatalytic reaction. Figure 10 shows the time-dependent

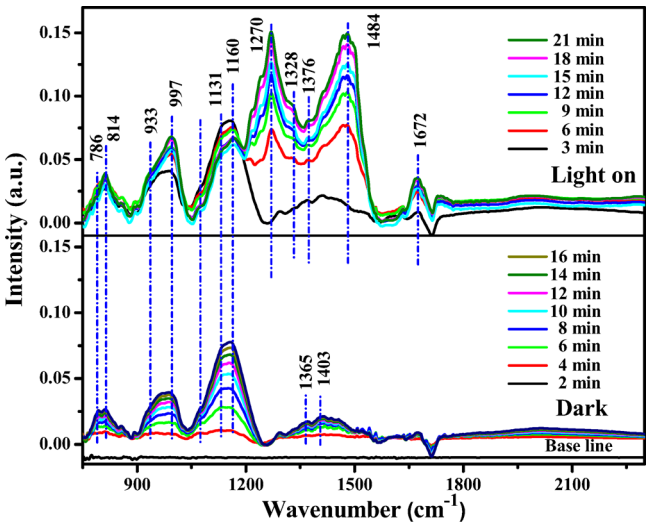

Figure 10. In situ FTIR spectra revealing the adsorption in the dark and photodegradation under light irradiation of NO over the surface of 3%Zn-BiOI.

in situ FTIR spectra of 3%Zn-BiOI, measured in the presence of NO + O_2 mixed gases in the dark and under visible light irradiation. Interestingly, the intensity of the FTIR peaks increases with increasing adsorption time in the dark, suggesting that some new species were generated after the contact of NO + O_2 molecules with the photocatalyst surface. In Figure 10, the bands at 1131 cm^{-1} can be assigned to NO[51] due to the physical adsorption of NO on Zn^{2+}-doped BiOI. The characteristic peaks of NO_2 were detected at 1365 and 786 cm^{-1}[51,52] because some of the NO was oxidized to NO_2 in the dark. Besides, the peaks assignable to bidentate and chelate nitrites (NO_2^-) can be seen at 814 and 1160 cm^{-1},[52,53] and the peaks belonging to bridging NO_3^- are located in the range 930−1000 cm^{-1} and at 1403 cm^{-1}[12,52] in the dark (Figure 10). The in situ FTIR results corroborate the charge difference distribution and adsorption of NO + O_2 over Zn^{2+}-doped BiOI. Thus, the following processes were possibly involved in the dark: (i) the adsorption of NO and O_2 on the surface of the photocatalyst, (ii) the oxidation of the adsorbed O_2 to O_2^- by OVs,[3] (iii) the reaction of O_2 with NO molecules to form NO_2,[54,55] and (iv) the direct interaction of NO and NO_2 with OVs and the reaction with O_2^- to form NO_2^- and NO_3^-.

The detailed mechanism of NO transformation on the surface of 3%Zn-BiOI in the dark is shown in Figure S10, and the possible reaction pathways are given in eqs 1−3:

$$O_2 + OVs \rightarrow 2O_2^- \quad (1)$$

$$2NO + O_2 \rightarrow 2NO_2 \quad (2)$$

$$2NO + O_2 + O_2^- \rightarrow c - NO_2^- + m - NO_3^- \quad (3)$$

During the photocatalytic reaction, new peaks also appeared. The peaks at 1270, 1328, 1484, and 1672 cm^{-1} can be assigned to bridging nitrites (br-NO_3^-),[13,56] monodentate nitrites (mo-NO_2^-),[39] and bidentate nitrites (bi-NO_3^-).[13] Obviously, the relative intensity of the peaks at 790, 933, 1131, and 1160 cm^{-1} becomes weaker with increasing irradiation time. In contrast, the intensity of the peaks belonging to br-NO_3^- (997 and 1270 cm^{-1}), mo-NO_2^- (1328 cm^{-1}), and bi-NO_3^- (1672 cm^{-1}) becomes stronger. The following reaction pathways can explain this observation. Upon visible light irradiation, the photo-generated electrons and holes were generated in 3%Zn-BiOI (eq 4). Subsequently, the photogenerated electrons reacted with the surface-adsorbed O_2 to form $\cdot O_2^-$ (eq 5). The photogenerated electrons also reacted with NO_2 to produce mo-NO_2^- (1328 and 1484 cm^{-1}) (eq 6). Simultaneously, the photogenerated holes could directly oxidize NO (1131 cm^{-1}) to bi-NO_3^- (1672 cm^{-1}) (eq 7). Besides, the produced chelate NO_2^- (814 and 1160 cm^{-1}) in the dark can be oxidized to more stable br-NO_3^- (997 and 1270 cm^{-1}) by $\cdot O_2^-$ under prolonged visible light irradiation (eq 8). Based on the above experimental and theoretical results, the mechanism for the photo-oxidative removal of NO by Zn^{2+}-BiOI photocatalyst after progress of adsorption is shown in Figure S11.

$$h\nu + Zn - BiOI \rightarrow e^- + h^+ \quad (4)$$

$$e^- + O_2 \rightarrow \cdot O_2^- \quad (5)$$

$$e^- + NO_2 \rightarrow NO_2^- \quad (6)$$

$$h^+ + NO + H_2O \rightarrow bi - NO_3^- + 2H^+ \quad (7)$$

$$2NO_2^- + \cdot O_2^- \rightarrow 2br - NO_3^- \quad (8)$$

Based on the above-presented experimental and theoretical results, the mechanism of the photo-oxidative removal of NO by the 3%Zn-BiOI sample is illustrated in Figure 11. The entire

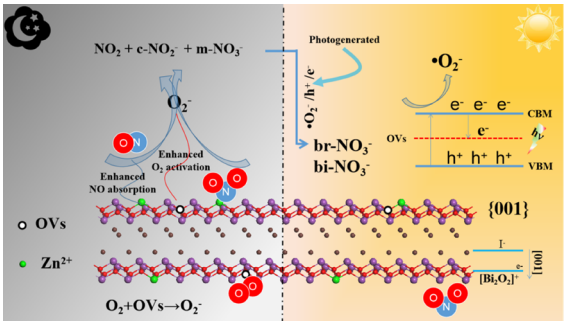

Figure 11. Schematic illustration of the photo-oxidative removal of NO by 3%Zn-BiOI in the dark and under visible light irradiation.

process can be divided into two parts: (i) reaction in the dark and (ii) reaction under visible light irradiation. In the dark, the NO + O_2 molecules are adsorbed on the surface of 3%Zn-BiOI to form stable coordinate bonds, which were confirmed by theoretical calculations and in situ FTIR in the dark. The simulation and calculation of the adsorption of NO and O_2 molecules on BiOI and Zn^{2+}-BiOI samples confirmed that the photocatalyst surface was enriched with NO by OVs, increasing the density of photo-active sites. This is an important step for the subsequent photocatalytic reaction. With the adsorption process of NO on the surface of Zn^{2+}-

DOI: 10.1021/acs.jpcc.9b03961
J. Phys. Chem. C 2019, 123, 16268−16280

BiOI being longer, the detailed process of the adsorption of NO on the photocatalyst surface was analyzed by in situ FTIR in the dark. Second, the concentration of OVs was increased by Zn^{2+} doping in the BiOI, which could capture the surface-adsorbed oxygen molecules to form O_2^-. The formed O_2^- was directly involved in the photo-oxidation of NO to NO_2, c-NO_2^-, and m-NO_3^-. According to the UV−vis spectroscopy results, the band gap of the Zn^{2+}-doped BiOI was tuned, and the OV level emerged. Upon visible light irradiation, electrons were excited from the VBM to the CBM of Zn^{2+}-BiOI. The recombination rate of photogenerated charge carriers was limited by the OV level in Zn^{2+}-BiOI. The photogenerated charge carriers migrate to the photocatalyst surface along the [001] direction under the influence of the built-in electric field force. On the photocatalyst surface, electrons were captured by the surface-adsorbed oxygen molecules to form $^{\cdot}O_2^-$ that oxidized NO to bi-NO_3^- and br-NO_3^-.

4. CONCLUSIONS

In summary, the 3D OV-rich Zn^{2+}-doped BiOI microspheres composed of highly exposed {001} ultrathin nanosheets were successfully synthesized by a simple one-step solvothermal method. The XPS and EPR results confirmed that Zn^{2+} could increase the concentration of OVs in BiOI. The photodegradation tests revealed that the higher concentration of OVs and the reduced thickness of the nanosheet resulting from Zn^{2+} doping could enhance the photocatalytic activity for NO removal. The photocatalytic activity for the photo-oxidative removal of NO over the 3%Zn-BiOI photocatalyst reached 53.6% under visible light irradiation. The calculation of interface adsorption revealed that OVs and Zn^{2+} can not only offer a donor energy level to extend the solar response range but also act as adsorption sites for NO and O_2 to optimize transfer capacity of surface charge carries. Hence, this work provides a detailed explanation for the photo-oxidative removal of NO by the OV-rich 3%Zn-BiOI photocatalyst.

■ ASSOCIATED CONTENT

Supporting Information

The Supporting Information is available free of charge on the ACS Publications website at DOI: 10.1021/acs.jpcc.9b03961.

Details of the photocatalytic activity test for NO removal, in situ FTIR study of photo-oxidation of NO, density functional theory (DFT) calculations, related analysis of the BiOI sample with only OVs, and detailed adsorption mechanism of NO in the dark condition (PDF)

■ AUTHOR INFORMATION

Corresponding Author

*E-mail: zgq2006@snnu.edu.cn. Tel/Fax: +86-29-81530750.

ORCID

Gangqiang Zhu: 0000-0001-5708-9446

Mirabbos Hojamberdiev: 0000-0002-5233-2563

Yu Huang: 0000-0003-3334-4849

Notes

The authors declare no competing financial interest.

■ ACKNOWLEDGMENTS

This work was supported by the National Natural Science Foundation of China (grant nos. 51772183 and 11847058), the Key Research and Development Program of Shaanxi Province (grant no. 2018ZDCXL-SF-02-04), and the Fundamental Research Funds for the Central Universities (grant nos. GK201903023 and GK201801005). M.H. would like to thank the Alexander von Humboldt (AvH) Stiftung for the research award.

■ REFERENCES

(1) Lu, Y.; Huang, Y.; Zhang, Y.; Cao, J. J.; Li, H.; Bian, C.; Lee, S. C. Oxygen Vacancy Engineering of Bi_2O_3/$Bi_2O_2CO_3$ Heterojunctions: Implications of the Interfacial Charge Transfer, NO Adsorption and Removal. *Appl. Catal., B* **2018**, *231*, 357−367.

(2) Han, J.; Zhu, G.; Hojamberdiev, M.; Peng, J.; Zhang, X.; Liu, Y.; Ge, B.; Liu, P. Rapid Adsorption and Photocatalytic Activity for Rhodamine B and Cr(VI) by Ultrathin BiOI Nanosheets with Highly Exposed {001} Facets. *New J. Chem.* **2015**, *39*, 1874−1882.

(3) Jia, Y.; Li, S.; Gao, J.; Zhu, G.; Zhang, F.; Shi, X.; Huang, Y.; Liu, C. Highly Efficient $(BiO)_2CO_3$-BiO_{2-x}-Graphene Photocatalysts: Z-Scheme Photocatalytic Mechanism for Their Enhanced Photocatalytic Removal of NO. *Appl. Catal., B* **2019**, *240*, 241−252.

(4) Barnes, J. M.; Apel, W. A.; Barrett, K. B. Removal of Nitrogen Oxides from Gas Streams Using Biofiltration. *J. Hazard. Mater.* **1995**, *41*, 315−326.

(5) Boubnov, A.; Carvalho, H. W. P.; Doronkin, D. E.; Günter, T.; Gallo, E.; Atkins, A. J.; Jacob, C. R.; Grunwaldt, J.-D. Selective Catalytic Reduction of NO over Fe-ZSM-5: Mechanistic Insights by Operando HERFD-XANES and Valence-to-Core X-ray Emission Spectroscopy. *J. Am. Chem. Soc.* **2014**, *136*, 13006−13015.

(6) Xu, H.; Wang, Y.; Cao, Y.; Fang, Z.; Lin, T.; Gong, M.; Chen, Y. Catalytic Performance of Acidic Zirconium-Based Composite Oxides Monolithic Catalyst on Selective Catalytic Reduction of NO_x with NH_3. *Chem. Eng. J.* **2014**, *240*, 62−73.

(7) Zhang, Q.; Huang, Y.; Xu, L.; Cao, J.-J.; Ho, W.; Lee, S. C. Visible-Light-Active Plasmonic Ag−$SrTiO_3$ Nanocomposites for the Degradation of NO in Air with High Selectivity. *ACS Appl. Mater. Interfaces* **2016**, *8*, 4165−4174.

(8) Zhao, Z.; Zhang, W.; Sun, Y.; Yu, J.; Zhang, Y.; Wang, H.; Dong, F.; Wu, Z. Bi Cocatalyst/Bi_2MoO_6 Microspheres Nanohybrid with SPR-Promoted Visible-Light Photocatalysis. *J. Phys. Chem. C* **2016**, *120*, 11889−11898.

(9) Ai, Z.; Ho, W.; Lee, S.; Zhang, L. Efficient Photocatalytic Removal of NO in Indoor Air with Hierarchical Bismuth Oxybromide Nanoplate Microspheres under Visible Light. *Environ. Sci. Technol.* **2009**, *43*, 4143−4150.

(10) Chen, M.; Huang, Y.; Lee, S. C. Salt-Assisted Synthesis of Hollow Bi_2WO_6 Microspheres with Superior Photocatalytic Activity for NO Removal. *Chin. J. Catal.* **2017**, *38*, 348−356.

(11) Chen, T.; Hao, Q.; Yang, W.; Xie, C.; Chen, D.; Ma, C.; Yao, W.; Zhu, Y. A Honeycomb Multilevel Structure Bi_2O_3 with Highly Efficient Catalytic Activity Driven by Bias Voltage and Oxygen Defect. *Appl. Catal., B* **2018**, *237*, 442−448.

(12) Shi, X.; Wang, P.; Li, W.; Bai, Y.; Xie, H.; Zhou, Y.; Ye, L. Change in Photocatalytic NO Removal Mechanisms of Ultrathin BiOBr/BiOI via NO_3^- Adsorption. *Appl. Catal., B* **2019**, *243*, 322−329.

(13) Li, X.; Zhang, W.; Li, J.; Jiang, G.; Zhou, Y.; Lee, S.; Dong, F. Transformation Pathway and Toxic Intermediates Inhibition of Photocatalytic NO Removal on Designed Bimetal@defective $Bi_2O_2SiO_3$. *Appl. Catal., B* **2019**, *241*, 187−195.

(14) Ou, M.; Dong, F.; Zhang, W.; Wu, Z. Efficient Visible Light Photocatalytic Oxidation of NO in Air with Band-Gap Tailored $(BiO)_2CO_3$−BiOI Solid Solutions. *Chem. Eng. J.* **2014**, *255*, 650−658.

(15) He, W.; Sun, Y.; Jiang, G.; Li, Y.; Zhang, X.; Zhang, Y.; Zhou, Y.; Dong, F. Defective Bi_4MoO_9/Bi Metal Core/shell Heterostructure: Enhanced Visible Light Photocatalysis and Reaction Mechanism. *Appl. Catal., B* **2018**, *239*, 619−627.

(16) Liu, L.; Jiang, Y.; Zhao, H.; Chen, J.; Cheng, J.; Yang, K.; Li, Y. Engineering Coexposed {001} and {101} Facets in Oxygen-Deficient

DOI: 10.1021/acs.jpcc.9b03961
J. Phys. Chem. C 2019, 123, 16268−16280

TiO_2 Nanocrystals for Enhanced CO_2 Photoreduction under Visible Light. *ACS Catal.* **2016**, *6*, 1097−1108.
(17) Ullah, H.; Tahir, A. A.; Mallick, T. K. Structural and Electronic Properties of Oxygen Defective and Se-Doped p-type $BiVO_4$(001) Thin Film for the Applications of Photocatalysis. *Appl. Catal., B* **2018**, *224*, 895−903.
(18) Wu, Y.; Han, Q.; Wang, L.; Jiang, X.; Wang, X.; Zhu, J. Room-Temperature Synthesis of BiOCl and $(BiO)_2CO_3$ with Predominant {001} Facets Induced by Urea and their Photocatalytic Performance. *J. Environ. Chem. Eng.* **2017**, *5*, 987−994.
(19) Cao, G.; Liu, Z. S.; Feng, P. Z.; Zhao, Y. L.; Niu, J. N. Concave Ultrathin BiOBr Nanosheets with the Exposed {001} Facets: Room Temperature Synthesis and the Photocatalytic Activity. *Mater. Chem. Phys.* **2017**, *199*, 131−137.
(20) Yang, H. G.; Sun, C. H.; Qiao, S. Z.; Zou, J.; Liu, G.; Smith, S. C.; Cheng, H. M.; Lu, G. Q. Anatase TiO_2 Single Crystals with a Large Percentage of Reactive Facets. *Nature* **2008**, *453*, 638−641.
(21) Wang, K.; Jia, F.; Zhang, L. Facile Construction of Low-Cost Flexible Solar Cells with p-type BiOI Nanoflake Arrays Fabricated via Oriented Attachment. *Mater. Lett.* **2013**, *92*, 354−357.
(22) Li, H.; Yang, Z.; Zhang, J.; Huang, Y.; Ji, H.; Tong, Y. Indium Doped BiOI Nanosheets: Preparation, Characterization and Photocatalytic Degradation Activity. *Appl. Surf. Sci.* **2017**, *423*, 1188−1197.
(23) Jamali-Sheini, F.; Cheraghizade, M.; Yousefi, R. Electrochemically Synthesis and Optoelectronic Properties of Pb- and Zn-Doped Nanostructured SnSe Films. *Appl. Surf. Sci.* **2018**, *443*, 345−353.
(24) Lu, C.; Wang, J.; Xu, F.; Wang, A.; Meng, D. Zn-Doped SnO_2 Hierarchical Structures Formed by a Hydrothermal Route with Remarkably Enhanced Photocatalytic Performance. *Ceram. Int.* **2018**, *44*, 15145−15152.
(25) Yang, S.; Lei, G.; Xu, H.; Xu, B.; Li, H.; Lan, Z.; Wang, Z.; Gu, H. A DFT Study of CO Adsorption on the Pristine, Defective, In-Doped and Sb-Doped Graphene and the Effect of Applied Electric Field. *Appl. Surf. Sci.* **2019**, *480*, 205−211.
(26) Zhang, Q.; Huang, Y.; Peng, S.; Zhang, Y.; Shen, Z.; Cao, J.-J.; Ho, W.; Lee, S. C.; Pui, D. Y. H. Perovskite $LaFeO_3$-$SrTiO_3$ Composite for Synergistically Enhanced NO Removal under Visible Light Excitation. *Appl. Catal., B* **2017**, *204*, 346−357.
(27) Ahmed, A.; Naseem Siddique, M.; Alam, U.; Ali, T.; Tripathi, P. Improved Photocatalytic Activity of Sr Doped SnO_2 Nanoparticles: A Role of Oxygen Vacancy. *Appl. Surf. Sci.* **2019**, *463*, 976−985.
(28) Liang, M.; Borjigin, T.; Zhang, Y.; Liu, B.; Liu, H.; Guo, H. Controlled Assemble of Hollow Heterostructured g-C_3N_4@CeO_2 with Rich Oxygen Vacancies for Enhanced Photocatalytic CO_2 Reduction. *Appl. Catal., B* **2019**, *243*, 566−575.
(29) Dong, G.; Jacobs, D. L.; Zang, L.; Wang, C. Carbon Vacancy Regulated Photoreduction of NO to N_2 over Ultrathin g-C_3N_4 Nanosheets. *Appl. Catal., B* **2017**, *218*, 515−524.
(30) Liu, X.; Iqbal, J.; Wu, Z.; He, B.; Yu, R. Structure and Room-Temperature Ferromagnetism of Zn-Doped SnO_2 Nanorods Prepared by Solvothermal Method. *J. Phys. Chem. C* **2010**, *114*, 4790−4796.
(31) Han, J.; Zhu, G.; Hojamberdiev, M.; Peng, J.; Liu, P. Synergetic Effects of Surface Adsorption and Photodegradation on Removal of Organic Pollutants by Er^{3+}-Doped BiOI Ultrathin Nanosheets with Exposed {001} Facets. *J. Mater. Sci.* **2016**, *51*, 2057−2071.
(32) Li, W.; Yu, R.; Li, M.; Guo, N.; Yu, H.; Yu, Y. Photocatalytical Degradation of Diclofenac by Ag-BiOI-rGO: Kinetics, Mechanisms and Pathways. *Chemosphere* **2019**, *218*, 966−973.
(33) Wang, K.; Li, Y.; Zhang, G.; Li, J.; Wu, X. 0D Bi Nanodots/2D Bi_3NbO_7 Nanosheets Heterojunctions for Efficient Visible Light Photocatalytic Degradation of Antibiotics: Enhanced Molecular Oxygen Activation and Mechanism Insight. *Appl. Catal., B* **2019**, *240*, 39−49.
(34) Wang, H.; Liang, Y.; Liu, L.; Hu, J.; Wu, P.; Cui, W. Enriched Photoelectrocatalytic Degradation and Photoelectric Performance of BiOI Photoelectrode by Coupling rGO. *Appl. Catal., B* **2017**, *208*, 22−34.
(35) Zhu, G.; Hojamberdiev, M.; Zhang, S.; Din, S. T. U.; Yang, W. Enhancing Visible-Light-Induced Photocatalytic Activity of BiOI Microspheres for NO Removal by Synchronous Coupling with Bi Metal and Graphene. *Appl. Surf. Sci.* **2019**, *467-468*, 968−978.
(36) Cui, D.; Wang, L.; Xu, K.; Ren, L.; Wang, L.; Yu, Y.; Du, Y.; Hao, W. Band-Gap Engineering of BiOCl with Oxygen Vacancies for Efficient Photooxidation Properties under Visible-Light Irradiation. *J. Mater. Chem. A* **2018**, *6*, 2193−2199.
(37) Ma, C.; Lin, Y.; Yang, H.; Tian, H.; Shi, L.; Zeng, J.; Li, J. Direct Observation of Magnetic-Ion Off-Centering-Induced Ferroelectricity in Multiferroic Manganite $Pr(Sr_{0.1}Ca_{0.9})_2Mn_2O_7$. *Adv. Mater.* **2015**, *27*, 6328−6332.
(38) Murphy, A. B. Band-Gap Determination from Diffuse Reflectance Measurements of Semiconductor Films, and Application to Photoelectrochemical Water-Splitting. *Sol. Energy Mater. Sol. Cells* **2007**, *91*, 1326−1337.
(39) Zhang, N.; Li, X.; Ye, H.; Chen, S.; Ju, H.; Liu, D.; Lin, Y.; Ye, W.; Wang, C.; Xu, Q.; et al. Oxide Defect Engineering Enables to Couple Solar Energy into Oxygen Activation. *J. Am. Chem. Soc.* **2016**, *138*, 8928−8935.
(40) Zhao, Y.; Zhang, J.; Wu, W.; Guo, X.; Xiong, P.; Liu, H.; Wang, G. Cobalt-Doped MnO_2 Ultrathin Nanosheets with Abundant Oxygen Vacancies Supported on Functionalized Carbon Nanofibers for Efficient Oxygen Evolution. *Nano Energy* **2018**, *54*, 129−137.
(41) Li, L.; Feng, X.; Nie, Y.; Chen, S.; Shi, F.; Xiong, K.; Ding, W.; Qi, X.; Hu, J.; Wei, Z.; et al. Insight into the Effect of Oxygen Vacancy Concentration on the Catalytic Performance of MnO_2. *ACS Catal.* **2015**, *5*, 4825−4832.
(42) Guo, J.; Liao, X.; Lee, M.-H.; Hyett, G.; Huang, C.-C.; Hewak, D. W.; Mailis, S.; Zhou, W.; Jiang, Z. Experimental and DFT Insights of the Zn-Doping Effects on the Visible-Light Photocatalytic Water Splitting and Dye Decomposition over Zn-doped BiOBr Photocatalysts. *Appl. Catal., B* **2019**, *243*, 502−512.
(43) Zhang, W.; Zhang, Z.; Kwon, S.; Zhang, F.; Stephen, B.; Kim, K. K.; Jung, R.; Kwon, S.; Chung, K.-B.; Yang, W. Photocatalytic Improvement of Mn-Adsorbed g-C_3N_4. *Appl. Catal., B* **2017**, *206*, 271−281.
(44) Rahman, J. U.; Nam, W. H.; van Du, N.; Rahman, G.; Rahman, A. U.; Shin, W. H.; Seo, W.-S.; Kim, M. H.; Lee, S. Oxygen Vacancy Revived Phonon-Glass Electron-Crystal in $SrTiO_3$. *J. Eur. Ceram. Soc.* **2019**, *39*, 358−365.
(45) Yang, W.; Yang, X.; Jia, J.; Hou, C.; Gao, H.; Mao, Y.; Wang, C.; Lin, J.; Luo, X. Oxygen Vacancies Confined in Ultrathin Nickel Oxide Nanosheets for Enhanced Electrocatalytic Methanol Oxidation. *Appl. Catal., B* **2019**, *244*, 1096−1102.
(46) Roychowdhury, R.; Dixit, V. K.; Vashisht, G.; Sharma, T. K.; Mukherjee, C.; Rai, S. K.; Kumar, S. Surface and Interface Properties of ZrO_2/GaAs, SiO_2/GaAs and GaP/GaAs Hetero Structures Investigated by Surface Photovoltage Spectroscopy. *Appl. Surf. Sci.* **2019**, *476*, 615−622.
(47) Jing, L.; Xu, Z.; Sun, X.; Shang, J.; Cai, W. The Surface Properties and Photocatalytic Activities of ZnO Ultrafine Particles. *Appl. Surf. Sci.* **2001**, *180*, 308−314.
(48) Huo, W. C.; Dong, X.'A.; Li, J. Y.; Liu, M.; Liu, X. Y.; Zhang, Y. X.; Dong, F. Synthesis of Bi_2WO_6 with Gradient Oxygen Vacancies for Highly Photocatalytic NO Oxidation and Mechanism Study. *Chem. Eng. J.* **2019**, *361*, 129−138.
(49) Liao, J.; Chen, L.; Sun, M.; Lei, B.; Zeng, X.; Sun, Y.; Dong, F. Improving Visible-Light-Driven Photocatalytic NO Oxidation over BiOBr Nanoplates through Tunable Oxygen Vacancies. *Chin. J. Catal.* **2018**, *39*, 779−789.
(50) Dong, X.'A.; Zhang, W.; Sun, Y.; Li, J.; Cen, W.; Cui, Z.; Huang, H.; Dong, F. Visible-Light-Induced Charge Transfer Pathway and Photocatalysis Mechanism on Bi Semimetal@Defective BiOBr Hierarchical Microspheres. *J. Catal.* **2018**, *357*, 41−50.
(51) Zhang, W.; Liu, X.; Dong, X.'A.; Dong, F.; Zhang, Y. Facile Synthesis of $Bi_{12}O_{17}Br_2$ and $Bi_4O_5Br_2$ Nanosheets: In Situ DRIFTS Investigation of Photocatalytic NO Oxidation Conversion Pathway. *Chin. J. Catal.* **2017**, *38*, 2030−2038.
(52) Wang, H.; Zhang, W.; Li, X.; Li, J.; Cen, W.; Li, Q.; Dong, F. Highly Enhanced Visible Light Photocatalysis and In Situ FT-IR

DOI: 10.1021/acs.jpcc.9b03961
J. Phys. Chem. C 2019, 123, 16268−16280

Studies on Bi Metal Defective BiOCl Hierarchical Microspheres. *Appl. Catal., B* **2018**, *225*, 218−227.
(53) Klingenberg, B.; Vannice, M. A. NO Adsorption and Decomposition on La_2O_3 Studied by DRIFTS. *Appl. Catal., B* **1999**, *21*, 19−33.
(54) Tang, N.; Liu, Y.; Wang, H.; Wu, Z. Mechanism Study of NO Catalytic Oxidation over MnO_x/TiO_2 Catalysts. *J. Phys. Chem. C* **2011**, *115*, 8214−8220.

DOI: 10.1021/acs.jpcc.9b03961
J. Phys. Chem. C 2019, 123, 16268−16280